OEA | Opto-Electronic Advances

Pixelated BIC metasurfaces for terahertz integrated sensing and imaging

Zhanqiang Xue†, Guizhen Xu†, Junliang Chen, Junxing Fan, Hongyang Xing, Ye Zhou*, Longqing Cong*

https://doi.org/10.29026/oea.2026.250211

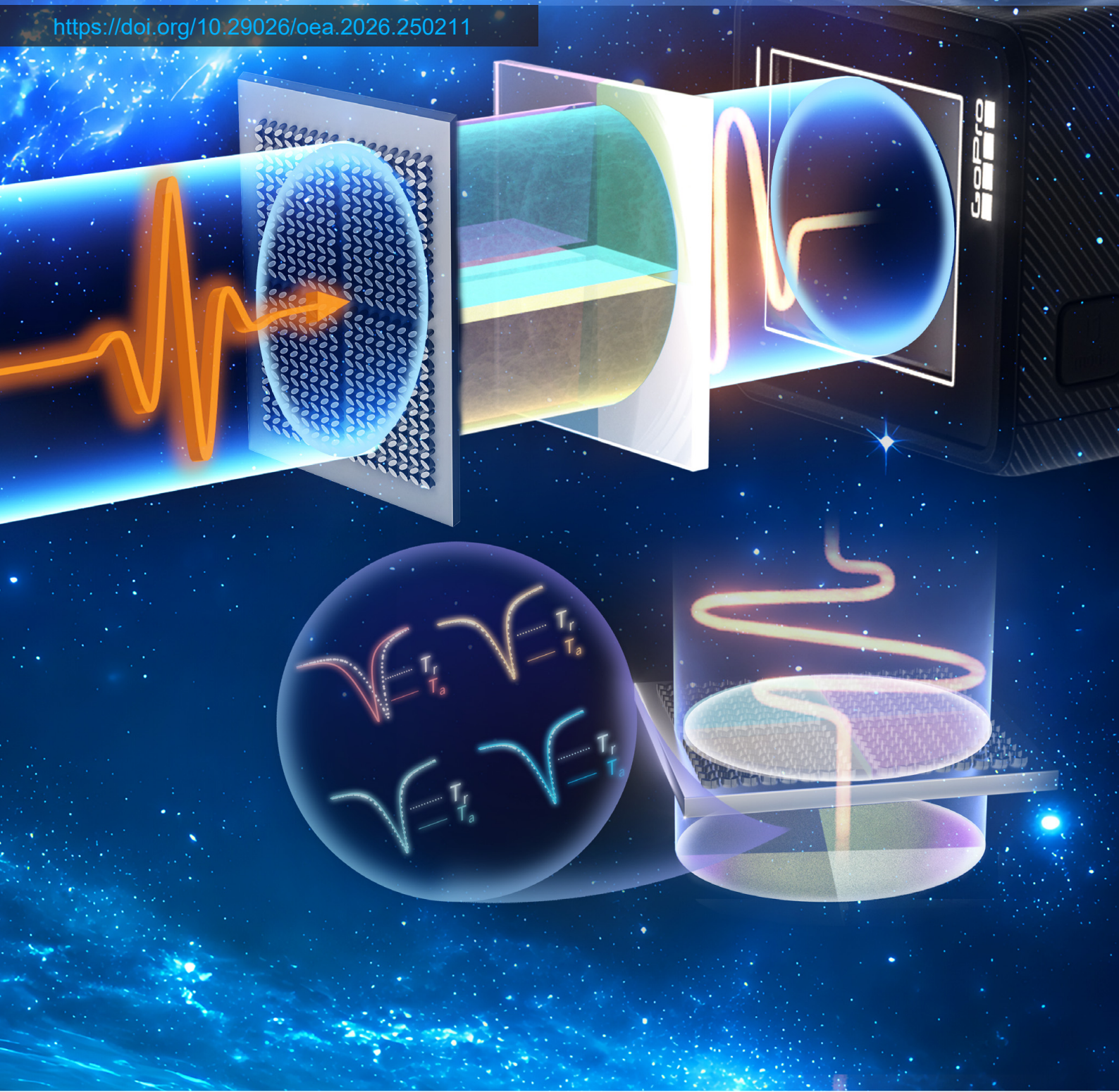

Opto-Electronic Advances

CN 51-1781/TN ISSN (Print) 2096-4579 ISSN (Online) 2097-3993

Pixelated BIC metasurfaces for terahertz integrated sensing and imaging

Zhanqiang Xue, Guizhen Xu, Junliang Chen, Junxing Fan, Hongyang Xing, Ye Zhou* and Longqing Cong*

Citation: Xue ZQ, Xu GZ, Chen JL, Fan JX, Xing HY, Zhou Y, Cong LQ. Pixelated BIC metasurfaces for terahertz integrated sensing and imaging. *Opto-Electron Adv* **9**, 250211 (2026).

https://doi.org/10.29026/oea.2026.250211

Received: 11 August 2025; Accepted: 2 December 2025; Published online: 10 February 2026

OEA | Opto-Electronic Advances

Article

March 2026, Vol. 9, No. 3

Open Access

Pixelated BIC metasurfaces for terahertz integrated sensing and imaging

Zhanqiang Xue[1†], Guizhen Xu[1†], Junliang Chen[1†], Junxing Fan[1], Hongyang Xing[1], Ye Zhou[2*] and Longqing Cong[1,3*]

Abstract: Conventional terahertz (THz) single-pixel imaging relies on a sequential process involving compressed sensing, which requires a spatial modulator and is often time-intensive. Here, we propose a new THz single-pixel imaging scheme operating in a parallelized fashion with a pixelated metasurface, demonstrated within a standard THz time-domain spectroscopy system. This approach encodes spatial information through multiple narrow linewidth resonances based on bound states in the continuum (BIC) physics, and the BIC-enabled pixelated metasurface facilitates the near-field distributed sensing through local field enhancement. We validate this integrated imaging and sensing capability using a 2×2 metasurface array in a proof-of-concept experiment, with scalability to larger arrays. The approach achieves 100% accuracy in binary imaging reconstruction from a single THz pulse and enables refractive index sensing with a sensitivity higher than 14.39 GHz/RIU. Leveraging the intrinsic penetration capability of THz radiation, this technique offers significant promise for next-generation noninvasive applications such as security inspection and defect detection in semiconductor chips and pharmaceutical products.

Keywords: bound states in the continuum; pixelated metasurfaces; terahertz photonics; integrated imaging and sensing

DOI: 10.29026/oea.2026.250211 | CSTR: 32247.14.oea.2026.250211

Citation: Xue ZQ, Xu GZ, Chen JL et al. Pixelated BIC metasurfaces for terahertz integrated sensing and imaging. *Opto-Electron Adv* **9**, 250211 (2026).

1 Introduction

Terahertz (THz) waves, characterized by low photon energy, broad bandwidth, and abundant fingerprint information, present substantial spectral advantages, facilitating diverse applications from chemical identification and material characterization to security screening and high-speed wireless communications[1–4]. In many of these advanced THz applications, imaging plays a critical role in mapping local invisible features of objects, such as detecting hidden defects in semiconductors or uncovering concealed drugs and explosives. However, conventional THz imaging techniques primarily rely on raster scan or computational methods due to the absence of large-area detector arrays, where a counterpart of charge coupled device (CCD) is missing in THz regime[5]. The inherent low photon energy of THz waves presents challenges in developing detectors capable of operating at room temperature, and most commercial THz detectors are either bulky or expensive, limiting their adaptability for large-area integration[6]. For instance, Ge:Ga photoconductor arrays require extremely low operating temperatures (0.3 K) to suppress thermal noise and achieve a sufficient signal-to-noise ratio[7]. While other detectors like field-effect sensors, pyroelectric detectors, and micro-radiometers can operate at room temperature, they often grapple with balancing sensitivity, bandwidth, and responsibility[8], and their large footprints and high costs further complicate integration in large-scale applications[5].

Under the constraint of the single-pixel detector in the current state-of-the-art THz apparatus, computational imaging techniques have been developed that leverage spatially modulated structured light on the targeted object, retrieving images through compressed sensing[9–11]. In this method, a sequential intensity profile, synchronized with the spatially modulated THz beam, is recorded by the single-

Received: 11 August 2025

Accepted: 2 December 2025

Published online: 10 February 2026

[1]State Key Laboratory of Optical Fiber and Cable Manufacture Technology, Department of Electrical and Electronic Engineering, Southern University of Science and Technology, Shenzhen 518055, China; [2]China-UK Low Carbon College, Shanghai Jiao Tong University, Shanghai 200240, China; [3]Guangdong Key Laboratory of Integrated Optoelectronics Intellisense, Southern University of Science and Technology, Shenzhen 518055, China.

†These authors contributed equally to this work.

*Correspondence: Y Zhou, E-mail: yezhou_lcc@sjtu.edu.cn; LQ Cong, E-mail: conglq@sustech.edu.cn

pixel detector lacking spatial resolution[12]. Spatial modulation[13–15] is typically achieved by incorporating active elements such as metallic masks[12], spinning disks[16], reconfigurable metamaterials[9], or digital micromirror devices[5]. This approach eliminates the need for large-scale detector array, enabling image reconstruction through computational algorithms. However, this comes at the expense of low framerates, as a mass of spatial light patterns must be projected and the subsequent imaging retrieval requires multiple iterations, making it time-consuming to generate a single frame. Achieving video-rate imaging at ~26 fps[17] remains a significant challenge under this computational single-pixel imaging scheme. Furthermore, the technique is typically limited to retrieving binary information, often losing material or spectral information about the target.

The broad bandwidth and ability to penetrate most dielectric materials of THz waves offer significant advantages for integrated sensing and imaging (ISAI), in analogy to the ongoing technical push for integrated sensing and THz communications (ISAC). Hyperspectral imaging enables a powerful toolkit for ISAI, allowing the simultaneous acquisition of both spectral and spatial information from targets. THz pulses have been applied in hyperspectral imaging with stochastic filters leveraging the broad bandwidth, where 25 or more filters are used to obtain convergent data through iterative processes, incorporating compressed sensing or deep learning algorithms[18,19]. However, the stochastic hyperspectral imaging lacks the ability to integrate the spectral sensing capability, where the spectral information is utilized to decrease the number of stochastic filters for imaging reconstruction. Recently, pixelated metasurfaces[20] have emerged as a novel class of spatial light modulators that are capable of reconstructing broadband spectrum incorporating CCDs operating in visible and infrared regimes[21] in a passive fashion. Moreover, they can enhance the local light-matter interactions and boost the capture of the fingerprints of analytes[22]. The pixelated metasurfaces demand a series of ultrasharp resonances spreading in a broad spectral range supported by the two-dimensional metasurface pixels (metapixels). For this purpose, advanced physics should be developed to support resonances possessing high quality factors (Q), large-range scalable frequencies, and a neat spectral background in the broad spectral range. Bound states in the continuum (BICs)[23–26] offer a systematic mechanism to engineer the resonances, which have gained considerable attention for applications in imaging[21], biosensing[22,27] and lasing[28,29]. Exploiting the Mie theory of dielectric scatterers, BIC-based metasurfaces have been shown to exhibit high-Q resonances[30] without additional resonance background —essential for spectrally selective enhancement across a broadband spectrum. These spectrally narrow and neat resonances can be directly correlated to specific spatial locations with a one-to-one correspondence so that spatial information can be encoded in and subsequently retrieved from the spectrum without the necessity of complex computation or data training processes.

Here, we report a scheme for integrated sensing and imaging using BIC-enabled pixelated metasurfaces in the THz regime. In the standard configuration of THz time-domain system with a single-pixel detector, we demonstrate single-pulse hyperspectral imaging in the far field and distributed sensing in the near field. The single-pulse ISAI is realized through the precise correlation between spectral resonances and spatial locations, facilitated by the powerful physics of BICs. Unlike conventional methods that rely on complex and time-intensive algorithms, and external active modulation apparatus, our approach allows spatial information of targets to be directly encoded into the broadband THz spectrum and processed in an all-optical and parallelized fashion with just one pulse, eliminating the need of raster scanning or sequential spatial light modulation. As a proof-of-concept demonstration, we experimentally validate the performance of single-pulse binary imaging and distributed sensing of refractive index with a 2×2 pixelated metasurface. The metapixels provide spectrally stable and traceable resonances whose intensities and frequency shifts characterize the local optical extinction and refractive indices of objects, respectively. The proposed method, which encodes spatial information into a frequency-multiplexed spectrum using pixelated metasurfaces in a single pulse, has the potential to reshape the paradigm of THz real-time imaging by enabling high framerate while simultaneously integrating distributed sensing capabilities.

2 Results

2.1 Principle of THz single-shot imaging

In the configuration of a THz time-domain system (THz-TDS), THz pulses are generated and coherently probed using commercially available single-pixel antennas. The emitted THz pulses are collimated by parabolic mirrors, interact with the samples, and are then collected by another set of parabolic mirrors for detection (see Supplementary information of Fig. S1). Within this setup, we illustrate the principle of the proposed THz single-pulse imaging, as schematically shown in Fig. 1. A specially designed pixelated metasurface (Fig. 1(a)) with spectral responses varying at different spatial locations is placed in the optical path of parallel beam. As THz pulses pass through, the metasurface encodes spatial information into a frequency-multiplexed distribution within the transmitted time-domain signals. In the same optical path, the imaging object is positioned behind the pixelated metasurface, where it is illuminated by the structured THz beam. The scattered signals, which contain object information, are collected by a coherent single-pixel detector. By performing a fast Fourier transform (FFT) and normalizing with reference signals (see Methods in the Supplementary information), the frequency-domain spectra are extracted. Each resonance frequency in the broadband spectrum corresponds precisely to a specific

spatial location on the metasurface, establishing a direct correlation between spectral and spatial information (Fig. 1(b)). When the imaging object interacts with the beam, the resonances at certain locations are modulated, which are captured by the single-pixel detectors within a single THz pulse (Fig. 1(e)). The spatial information of the object is reconstructed by reading the variations in resonance intensity in the frequency-domain spectra (Fig. 1(d)).

In order to numerically recognize the spatial distribution of targets, a criterion is defined by quantifying the transmission intensity difference $\Delta T_{\rm i}(\omega) = |T_{\rm oi}(\omega) - T_{\rm r}(\omega)|/\Delta I_{\rm i}$ where $T_{\rm r}(\omega)$ represents transmission intensity spectrum of the pixelated metasurface, $T_{\rm oi}(\omega)$ is the transmission spectrum of resonance #i modulated by the object, and $\Delta I_{\rm i}$ is the peak-to-peak intensity of resonance induced by metapixel #i. For binary imaging, a numerical threshold of 0.5 is applied. The threshold is used to classify the corresponding imaging pixel as either THz transparent ("1" when $\Delta T_{\rm i} \geq 0.5$) or opaque ("0" when $\Delta T_{\rm i} < 0.5$), which allows for the spatial distribution of the imaging object to be numerically identified based on the analysis of the intensity difference spectra (Fig. 1(f)).

The proposed imaging principle completes one-frame acquisition with a single-shot THz pulse, processing the information in a parallelized fashion through frequency multiplexing by leveraging the broadband spectral characteristics of THz waves. The method eliminates the need for a raster scanning process in conventional imaging configurations or sequential spatial light modulation in compressed sensing[5]. The process operates in an all-optical approach, removing mechanical components and external electrical modulators. As a result, the imaging framerate is solely determined by the THz pulse repetition rate, which is 24 Hz using the Menlo systems TeraSmart (> 6.0 THz bandwidth), making it suitable for real-time display. The imaging resolution is defined by the number of metapixels as well as the resonance density loaded within the available bandwidth. In the absence of noise from mechanical or electrical modulation components, the all-optical imaging configuration will

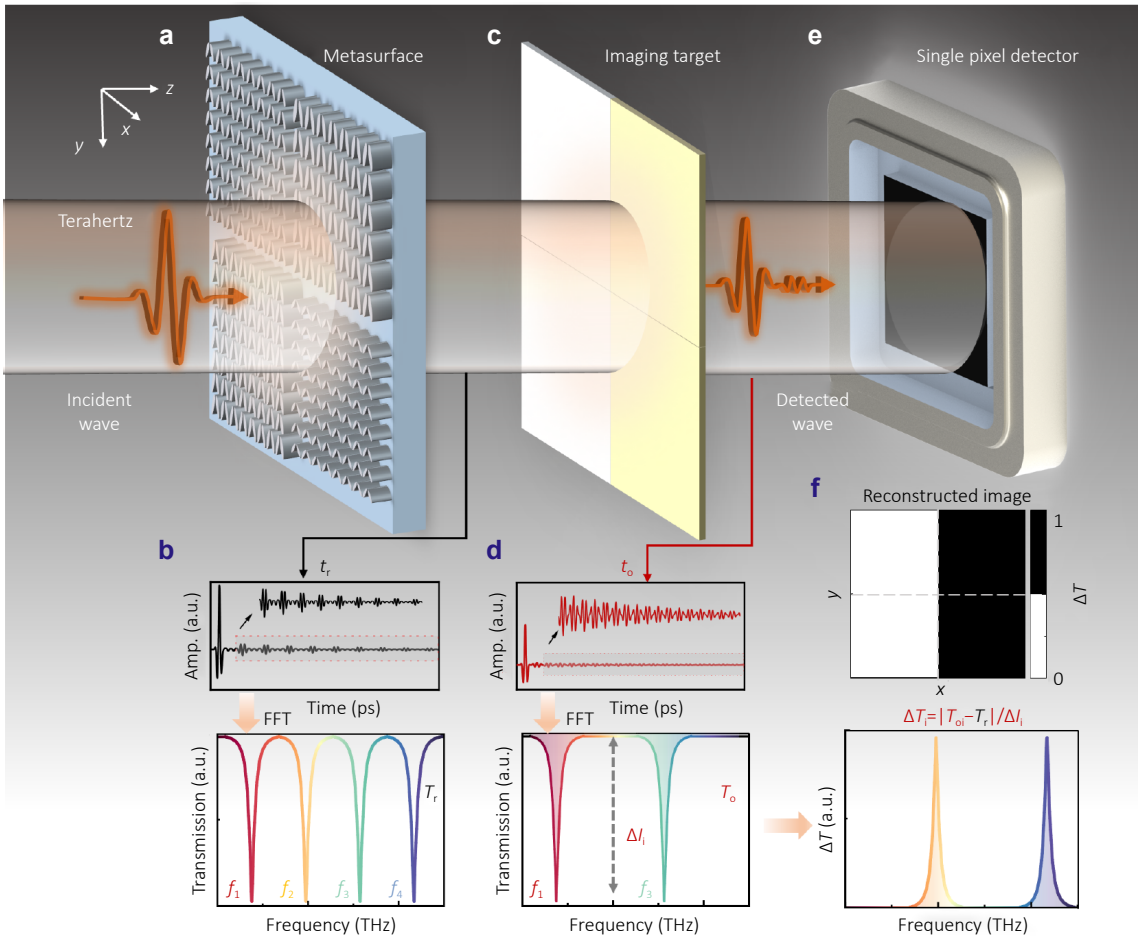

Fig. 1 | Principle of THz single-shot imaging using a pixelated metasurface. (a) Configuration of a 2×2 pixelated dielectric metasurface that supports four resonances at different frequencies. (b, d) Transmitted time-domain and frequency-domain spectra through the pixelated metasurface and the object, respectively. (c) Schematic of the imaging target with distributions of THz transparent and opaque regions. (e) Single pixel detector to collect the multiplexed time-domain signals. (f) Intensity difference spectrum carrying the spatial information of the imaging target, and the reconstructed binary image.

significantly improve imaging quality and system stability.

2.2 BIC-empowered pixelated dielectric metasurface

The core component in the proposed imaging scheme is the pixelated metasurface, which encodes spatial information into broadband THz pulses. The incoherence of resonances across the different metapixels is crucial to ensure no crosstalk between them. This requires each metapixel to support a clean resonance within a broadband frequency range with a narrow linewidth and scalable central frequency. The powerful physics of BICs offers an ideal solution for this purpose, as their resonance linewidth is customizable, from a finite value (quasi-BIC) to zero, and the resonance frequency can be tuned via geometrical parameters and the dispersion relation[31]. By employing the unit cell composed of a pair of tilted elliptical silicon pillars as shown in Fig. 2(a), a quasi-BIC resonance is achieved. The symmetry-protected BIC properties are verified by the infinite Q when the tilting angle θ is tuned to zero (Fig. 2(b)). A comprehensive theoretical analysis is provided in the Supplementary information of Section 2, rigorously establishing the nature of the observed quasi-BICs through both symmetry classification and multipolar decomposition. As the tilting angle (θ) increases, breaking the C_2 symmetry causes bounded photons to leak into free space, resulting in a Q factor that follows an inverse quadratic dependence on the asymmetry degree ($Q \propto \sin^{-2}(\theta)$)[32]. The quasi-BIC resonance, with clean spectral characteristics covering the frequency range from 0.55 to 0.75 THz and narrow linewidth, can be shifted across a large extent of frequencies by scaling the geometrical parameters of the unit cells[32] (see Supplementary information of Fig. S5). The spectral evolution versus tilting angle is evident from the far-field transmission spectra, where broadening linewidths and frequency shift are observed in Fig. 2(c). The local electric field distributions at the resonance frequency for a tilting angle of θ = 10° (Fig. 2(d)) show that, unlike guided-mode resonances, the quasi-BIC resonance significantly enhances the local field in the gap between the pillars. The enhanced localized fields are critical for surface-enhanced sensing.

As a proof-of-concept demonstration, we fabricated the BIC-empowered pixelated metasurfaces, with optical microscopic images shown in Fig. 2(e). The metasurfaces were fabricated using conventional photolithography based on 80 μm-thick high-resistivity silicon (dielectric constant ε = 11.7). After patterning the photoresist, deep reactive ion beam etching (Deep RIE) was carried out, leaving the

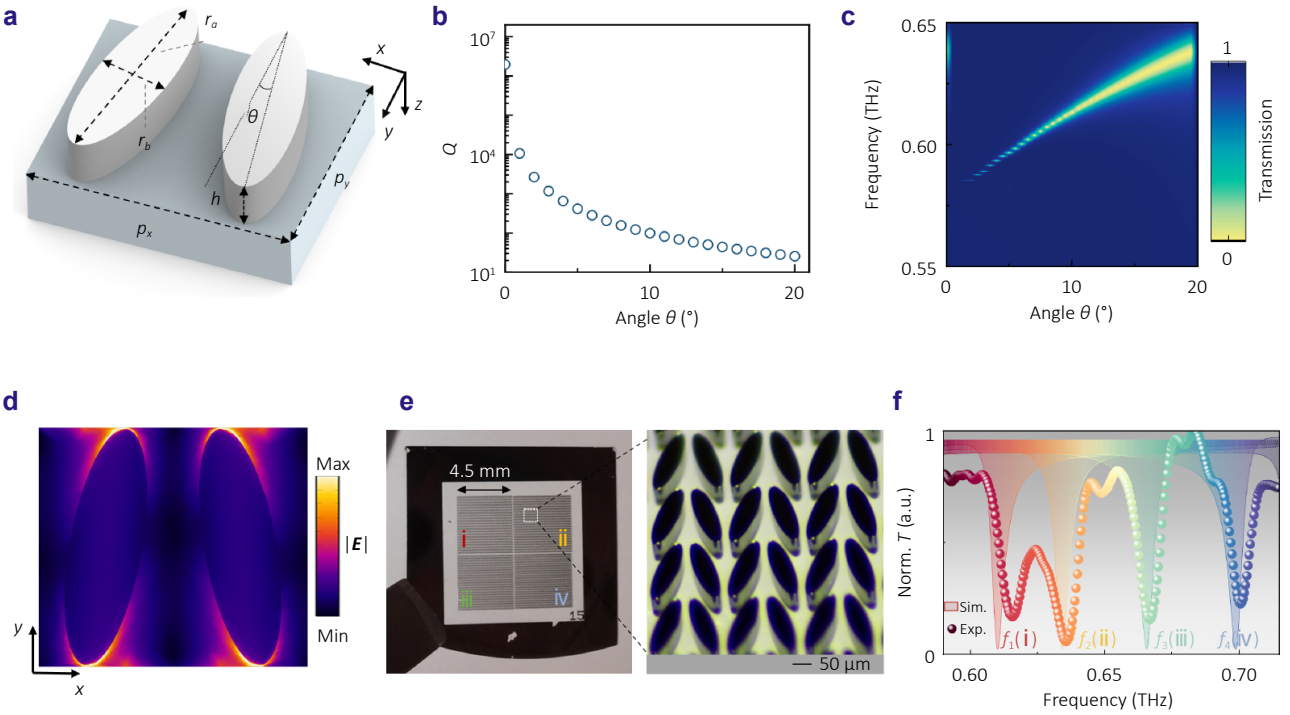

Fig. 2 | BIC-empowered pixelated dielectric metasurface. (a) Schematic diagram of a unit cell comprised of tilted elliptical silicon pillar pair on a quartz substrate. The geometrical parameters are r_a =176 μm, r_b = 54 μm, P_x = 200 μm, P_y = 177 μm, and h = 80 μm. (b, c) Simulated Q factors and transmission intensity spectra versus tilting angles ϑ. (d) Electric field distributions of quasi-BIC resonance at the resonance frequency with tilting angle ϑ = 10°. (e) Optical microscopic images of the fabricated multipixel dielectric metasurface. The excellent fabrication quality is observed in the zoomed-in microscopic image of the sample. (f) Normalized measured (dots) and simulated (shaded lines) transmission intensity spectra. The four metapixels are measured in a parallel fashion in a single-shot pulse, and the simulated spectra are calculated independently for each metapixel with periodic boundary conditions. Loss-free silicon and quartz are used in simulations.

elliptical silicon pillar pairs attached on a 200 μm-thick quartz substrate (see Methods in the Supplementary information). The geometry parameters of the 2×2 metapixels were optimized by using simulations to produce spectrally independent resonances at different frequencies, exhibiting nearly uniform frequency spacing (f_1–f_4, at 0.61 THz, 0.63 THz, 0.67 THz and 0.70 THz) and similar linewidths ($Q \approx 100$ in simulations, as detailed in Supplementary information of Table S2). Figure 2(f) compares the simulated transmission spectra of each isolated metapixel with the spectra measured from the pixelated metasurface in parallel in a single THz pulse. The excellent agreement between simulations and experiments confirms the precision of the fabrication, although the measured spectra show slightly larger linewidths attributed to the finite size of metapixels and scattering losses from fabrication imperfections. The pixelated metasurface establishes a precise one-to-one correspondence between the spatial locations of the metapixels (i–iv) and their spectral resonances (f_1–f_4), which would effectively modulate THz pulses and encode spatial information within the frequency domain.

2.3 Far-field single-shot binary imaging

Following the analysis and experimental characterization of quasi-BIC metapixels, we validate the performance of the proposed THz single-pixel imaging scheme in the far-field measurements using THz-TDS based on the pixelated metasurfaces. A series of imaging objects were prepared, utilizing a polytetrafluoroethylene (Teflon) board as the substrate (transparent to THz waves) with structured aluminum foil (opaque to THz) attached to the board, as schematically illustrated in Fig. 3(a) (also see Supplementary information of Fig. S8). The imaging setup measured one single-pulse THz signal before and after placing the object in the THz optical path. The corresponding transmission intensity spectra, obtained after performing FFT, are displayed in Fig. 3(b), where the grey-shaded spectrum represents the spatially encoded THz spectrum, and the colored line shows the modulated signals by the object, respectively (see Methods in the Supplementary information).

For the imaging target with a specific distribution, the frequency-domain signals reveal clear contrasts in resonances at frequencies f_1 and f_4, encoding spatial information related to metapixels #i and #iv, respectively. Spatial information was retrieved using the intensity difference spectra $\Delta T_i(\omega)$, as shown in Fig. 3(c), with the spatial correlation to each metapixel clearly visualized. By applying the binary threshold of 0.5, the image was reconstructed with high contrast and perfect accuracy (Fig. 3(d)), demonstrating the efficacy of the frequency-multiplexing strategy to overcome the bottleneck of low signal-to-noise ratio in the current apparatus. The binary imaging measurements were conducted in the far-field regime, ensuring that the mode properties of each metapixel remained intact without resonance frequency shifts during the imaging process. Minor deformations of resonance lineshapes come from weak coupling between neighboring resonances, but these effects are negligible compared to the modulation induced by the target pixels. Therefore, the intensity modulation at each

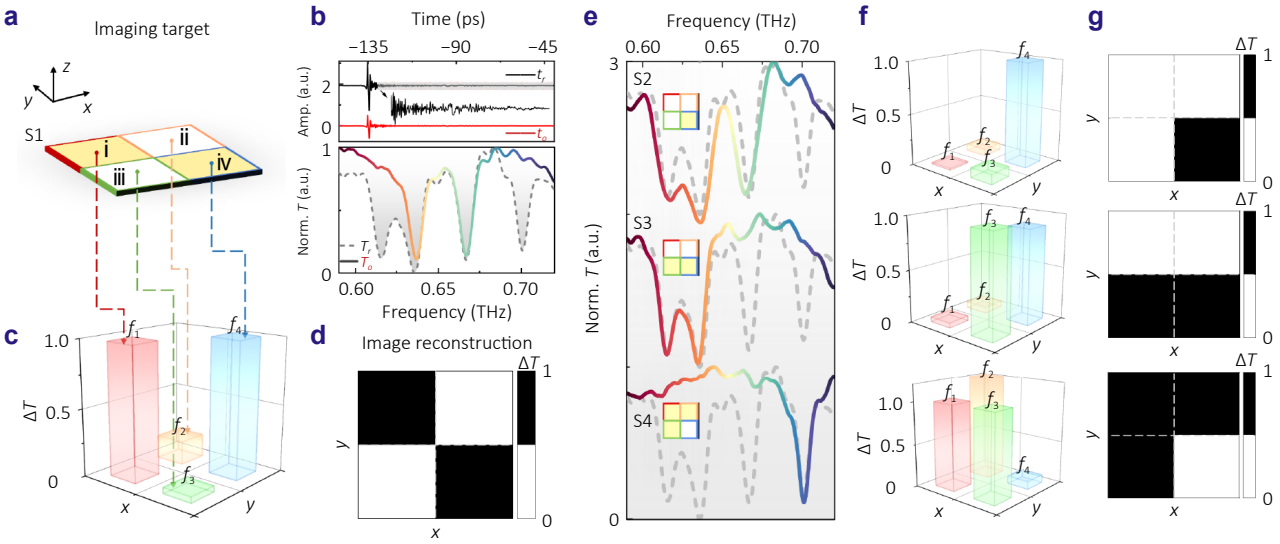

Fig. 3 | Far-field single-shot binary imaging. (a) Schematic of the imaging target. The yellow areas indicate the THz opaque pixels, while the white parts represent THz transparent pixels. (b) Measured single-shot THz time domain signals and normalized transmission intensity spectra of reference and target after performing FFT. The shaded envelope is transmission spectrum of the frequency-multiplexing THz beam passing through a Teflon substrate, serving as the reference in the background. The colored line is measured spectrum through target. Δ*T* denotes the difference of spectral intensity. (c) Target spatial distribution retrieval according to the discrete variation of resonances. (d) Reconstructed image of the target from a single-shot measurements. (e–g) Imaging experiment results with targets of different distributions.

resonance is purely linked to the overall transmittance or extinction coefficient of each pixel in the target.

The accuracy and versatility of the single-shot binary imaging scheme were further demonstrated with imaging targets of all possible spatial distributions (Fig. 3(e–g) and Supplementary information of Fig. S10). Under the same measurement condition, the reconstructed images match the target with 100% accuracy, demonstrating reliability and eliminating common errors inherent in conventional computational imaging. Although the proof-of-concept experiments were performed using a 2×2 pixelated metasurface, the proposed far-field imaging scheme is scalable to large-scale arrays by reducing the metapixel size and enlarging the THz beam spot. Expanding spectral multiplexing capabilities would depend on increasing the resonance density with narrower linewidths for each metapixel and broadening clean spectral bandwidth of quasi-BIC resonances. This will enable the integration of more spatial information into a single THz pulse, making this technique a promising avenue for large-scale real-time THz imaging. Furthermore, we increased the object-metasurface distance to experimentally evaluate how diffraction at larger separations impacts single-shot binary imaging (Fig. S12). These results confirm that our pixelated metasurface retains its imaging capability over a range of distances, with only gradual degradation at larger separations.

As a direct application, we experimentally demonstrated the capability of our system to resolve the contour of a concealed metallic object, leveraging the penetrative nature of THz radiation, as illustrated in Fig. 4(a). More detailed information of the object's size, position, and relative alignment with the beam is provided in Fig. S13. A surgical blade with a simple contour, enclosed within an opaque envelope and invisible to the naked eye, was positioned vertically behind the pixelated metasurface. Transmission spectra were recorded at various lateral positions by translating the envelope horizontally by a distance d, allowing us to probe two distinct regions near the blade's edge (Fig. 4(b) and 4(c)). Using the same spectral retrieval methodology described earlier, we mapped the spatial distribution of spectral modulation across the metasurface. To enhance the imaging resolution, we introduced an additional modulation threshold (grey: $0.2 \leq \Delta T_i(\omega) \leq 0.5$), representing partially blocked metapixels. Fully blocked pixels (black: $0.5 < \Delta T_i(\omega) \leq 1$) correspond to regions where the blade occludes the incident THz radiation. From these measurements, and with knowledge of the blade's orientation, we estimated the position and contour of the concealed blade, as shown in Fig. 4(d). By acquiring spectra at more spatial locations and incorporating finer grayscale levels, the contour reconstruction can be further refined, offering a fast, noninvasive method for identifying concealed hazardous metallic objects.

2.4 Near-field single-shot distributed sensing

The high Q factors and accompanying local field enhancement of quasi-BIC resonances (Fig. 2(d)) lead to significantly improved light-matter interactions. This provides a crucial platform for lasing[29,33], nonlinear photonics[34,35], and biosensing[36,37], phase singularity sensing[38]. By capitalizing on the near-field enhancement in the vicinity of air gaps of metapixels, we explored the distributed sensing capability of the pixelated metasurface, as illustrated in Fig. 5(a). In this configuration, the typical quasi-BIC resonances undergo a linear frequency shift proportional to changes in the refractive index of analyte ($\Delta f_i \propto \Delta n_i$)[39]. The pixelated metasurface, acting as both a spatial and spectral modulator, enables the retrieval of the spatial distribution of the refractive index of the analyte. This is achieved by tracking the resonance

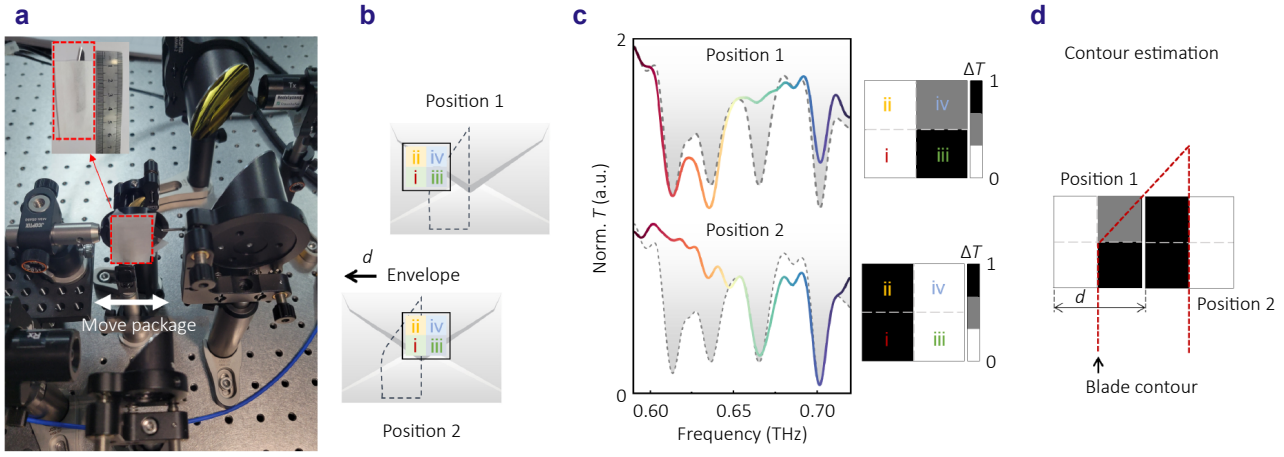

Fig. 4 | Generalized single-shot imaging for concealed metallic objects within a package. (a) Imaging setup. The concealed blade in an envelope is placed behind the metasurface. (b) Two imaging positions by translating the envelope horizontally with a distance d. (c) THz transmission spectra measured at the two chosen positions. (d) Reconstructed image of the hidden metallic target derived from two single-shot measurements.

frequencies encoded with spatial information, leveraging the same mechanism used in the imaging process (Fig. 5(a)).

The accurate retrieval of the local refractive index relies on the known sensitivity (S) of each metapixel, which is a pivotal metric for quantifying how the resonances respond to changes in the refractive index. The sensitivity is defined as

$$S = \frac{\Delta f}{\Delta n}, \tag{1}$$

where Δf represents the shift in resonance frequency, and $\Delta n = n_a - n_{ref}$ is the change in refractive index, with n_a and n_{ref} denoting the indices of analytes and reference air, respectively. Using the same 2×2 pixelated metasurface as a proof-of-concept demonstration, we experimentally characterized the sensitivity of each metapixel. A distinguishable frequency shift is observed by coating metapixel #iv with a 50 μm-thick polyimide (PI, n = 1.66) layer, compared to the reference spectrum of air as shown in Fig. 5(b). To clearly resolve the frequency shifts, resonances with narrower linewidths are preferred, as they enable more precise detection of the refractive index changes. This highlights the importance of high-Q resonances in enhancing sensing performance.

Following the same process, analytes with different indices were coated at an identical thickness (50 μm) on the pixelated metasurface, and the frequency shifts for the four metapixels were recorded and summarized in Fig. 5(c). In experiments, polydimethylsiloxane (PDMS, n = 1.41), polytetrafluoroethylene (PTFE, n = 1.46), and polyimide (PI, n = 1.66) were adopted to characterize the sensitivity (see Supplementary information of Fig. S17(a)). From the linear fitting of the frequency shifts (see Supplementary information of Table S3), the sensitivities of the four metapixels were determined (Fig. 5(d) and Supplementary information of Table S4). Note that the sensitivity was measured with an analyte thicker than the saturated value to ensure that thickness variations do not affect the resonance frequency (see Supplementary information of Fig. S18). In this context, a requirement of the analyte thickness larger than the saturated value is essential for the accurate retrieval of the local refractive index. The measured spectra could resolve the refractive index variations between PDMS and PTFE from the frequency shift based on metapixel #iv (see Supplementary information of Fig. S17). The sensing resolution could be improved by using metapixels with higher Q factors[40]. A comparison of the imaging and sensing performance with existing pixelated metasurface platforms is provided, with key performance parameters, including resonance Q-factor, resonance number, and spectral range summarized in Tables S5 and S6.

The distributed sensing capabilities of the pixelated metasurface were experimentally demonstrated in single-pulse

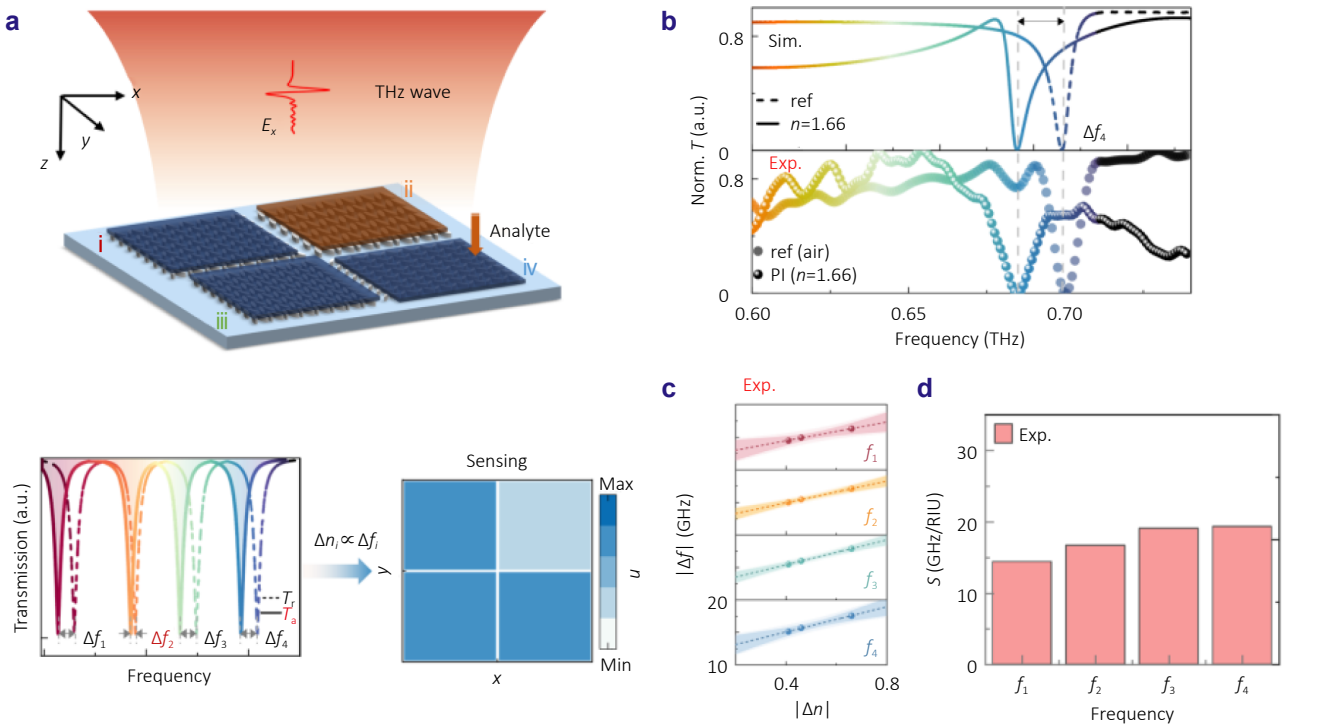

Fig. 5 | Near-field single-shot distributed sensing. (a) Schematic diagram of pixelated metasurfaces for distributed sensing where the analyte is coated on the pixelated metasurface, and spatial variation of the index is retrieved from the spatial-encoded resonances obtained through a sing-shot THz measurement. (b) Simulated (top) and experimental (bottom) transmission spectra of metapixel #iv coating with and without 50 μm-thick PI film. (c) Experimental frequency shifts of the four metapixels. The solid and dashed lines represent the linear fitting to the simulated and experimental data, respectively, using the equation $y = ax + b$, where a and b are constants. (d) Summary of the sensitivities (S) of the four metapixels.

measurements (Fig. 6). Analytes with distributed indices were coated on the pixelated metasurface (air, PDMS, and PI, Fig. 6(a)), and transmission spectra were measured using a single THz pulse. Figure 6(b) displays the frequency-domain intensity spectra for three types of index distribution measurements, where the background is the reference spectra of the pixelated metasurface with uniformly coated analytes of air (grey), PI (purple), or PDMS (blue) for a comparison.

The index distributions of unknown samples can be recognized by matching the central frequencies of the measured spectra to the background spectra of uniformly coated analytes. In the first type of index distribution measurement, frequency shifts (Δf) relative to reference spectrum of air-coated pixelated metasurface are determined for each metapixel (Fig. 6(c)) and the refractive index distributions of analyte are established by consulting a look-up table of metapixel sensitivities (Fig. 6(d)). The retrieved index distribution of [1.63, 1.66, 1.66, 1.00] matches the predesigned sample well, where metapixels #i, #ii, and #iii are covered with PI leaving metapixel #iv with air. Similar results [1.63, 1.66, 1.00, 1.00] were achieved with another type of index distribution measurement (middle row of Fig. 6).

The capability to detect low-contrast refractive index distributions was demonstrated in the third type of spatial index measurement, where analytes with similar indices were coated on the pixelated metasurface (third row of Fig. 6). The measured spectrum reveals the recognizable frequency shifts for the four resonances, and the retrieved spatial index distribution of [1.63, 1.66, 1.42, 1.41] accurately reflects the predesigned configuration coated by PI and PDMS. In the proposed near-field distributed sensing scheme, the accuracy of local refractive index retrieval is primarily limited by the frequency resolution and stability of the measurement apparatus.

As a practical application of distributed sensing utilizing the nondestructive and penetrative properties of THz waves, we envision how this technique can be employed to detect hidden defects in high-quality silicon chips with high spatial resolution. By monitoring local variations in the refractive index, the presence of defects, such as embedded invisible pores, can be captured, as schematically illustrated in Fig. S19. For a typical silicon chip (n = 3.42), the detection of defects as small as 2% of the volume is possible based on the sensitivity according to the effective medium theory[41]. Given the current spatial resolution, which is determined by the area of each metapixel, defects on the scale of the probing wavelength can be detected. The resolution of distributed sensing could be further enhanced to detect defects much smaller than the wavelength. This improvement can be achieved through two primary approaches: by improving the frequency resolution of the THz-TDS, and by reducing the size of each metapixel while simultaneously improving sensitivity.

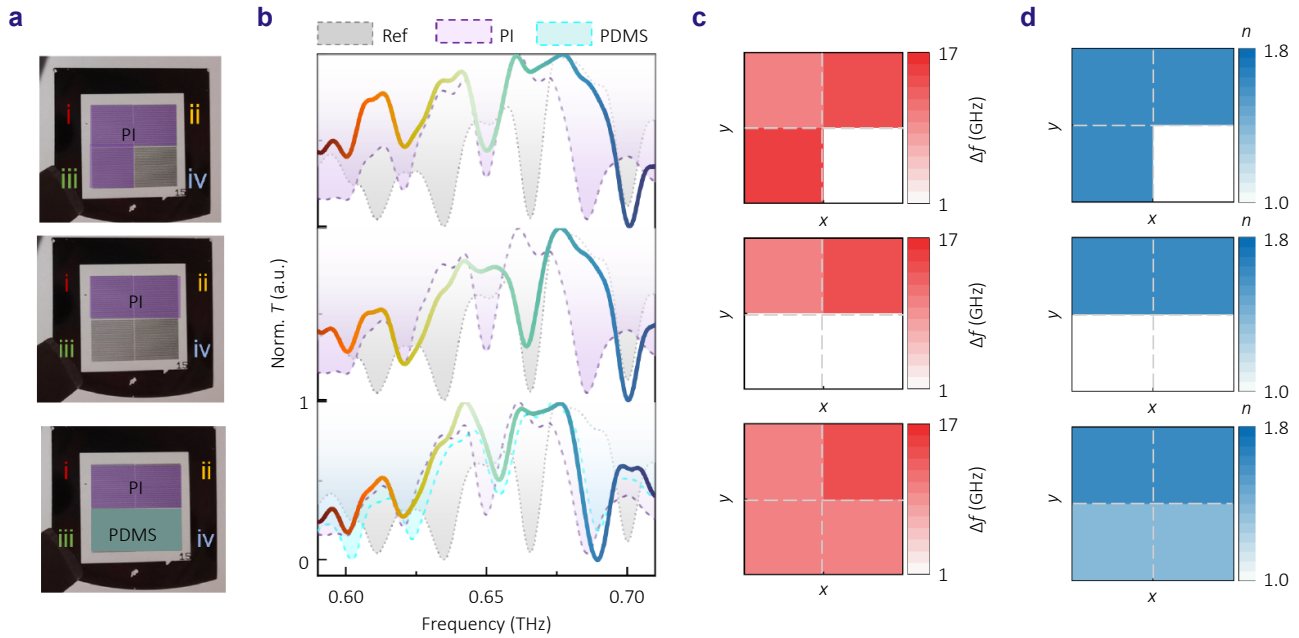

Fig. 6 | Experimental results of near-field single-shot distributed sensing. (a) Optical images of pixelated metasurface coated by different distributions of analyte. The purple and green shaded areas represent PI and PDMS, respectively. (b) Experimental transmission spectra to discern the spatial distributions of the analyte. The solid lines indicate the transmission spectra of samples coated by analytes. The shaded spectra represent the references when samples are coated by uniform air (grey), PI (purple), and PDMS (green), respectively. (c) Spatial frequency shift distributions of the four resonances from experimental spectra. (d) Spatial index distributions according to frequency shift and linear sensitivity.

3 Conclusions

We have demonstrated the versatile and powerful capabilities of BIC-enabled pixelated metasurfaces from both far-field binary imaging and near-field distributed sensing in a commercial THz-TDS. In these approaches, spectral intensity and frequency shifts serve as additional degrees of freedom to characterize local extinction and refractive index variations of target objects, respectively, while preserving the inherent coherence advantages of time-domain spectroscopy. When combined with raster scanning, the proposed scheme enables a fourfold improvement in spatial resolution based on the current metasurface design.

Notably, during near-field sensing, slight intensity modulation was observed attributed to two factors: intrinsic absorption from the analyte (nonzero imaginary part of the refractive index) and coupling between the neighboring resonances. Despite these perturbations, central frequencies can be accurately retrieved for precise refractive index detection. On the other hand, the ISAI performance is primarily obstructed by the frequency resolution, signal-to-noise ratio, and repetition rate of the THz-TDS. To advance this technology, the next step involves increasing the number of metapixels while addressing a key challenge: the trade-off between the Q factors and the area of the metapixels for quasi-BIC resonances. Scaling to larger multi-pixel arrays (e.g., 8×8, Figure S16) is feasible in simulation but imposes more stringent constraints on material thickness. A deeper understanding of BIC physics is necessary to address these constraints. In terms of distributed sensing, enhancing the sensitivity of metapixels is crucial for detecting tiny defects, such as pores or impurities in semiconductors, integrated circuits, and pharmaceuticals. Increasing the frequency spacing between neighboring resonances could mitigate spectral coupling effects on intensity modulation and extend the sensing range for distributed index changes.

Most prior THz imaging approaches, which are often enhanced by algorithms or deep learning[42–44], rely heavily on active hardware, spatial light modulators, or mechanical raster scanning for image reconstruction. These active components introduce additional instability, noise, and tremendous time consumption with a sequential process. In contrast, our proposed scheme integrates sensing and imaging into a streamlined, compact platform compatible with commercial THz-TDS. The scheme eliminates the need for high-power pump beams, complex optical paths, external driving components, or bulky mechanical components. The ISAI capability is achieved in a single THz pulse, with imaging reconstruction performed in a parallel, all-optical manner. Without auxiliary computation reconstruction, the spatial distributions of binary imaging and material properties are directly and immediately mapped in the spectral domain, reducing both error probability and time consumption. In the proof-of-concept experiments, we demonstrated 100% accuracy in binary imaging and achieve a sensitivity higher than 14.39 GHz/RIU in distributed sensing. This highlights the significant potential of the proposed approach for real-time ISAI applications, particularly in next-generation security screening and quality inspection, where the non-destructive and penetrative properties of THz radiation can be fully utilized.

4 Materials and methods

Fabrication. We first bonded an 80 μm thick high-resistance silicon to a quartz substrate using adhesive (NOA74). The bonded samples were placed in a UV box (wavelength 365 nm) precuring for 10 seconds at 150 W, followed by a final cure for 300 seconds at 300 W. The bonded samples were cut into square pieces of 17 mm × 17 mm, which is necessary for uniform heat dissipation in the subsequent etching processes. A 1.5 μm thick photoresist layer (S1818) was spin-coated on top of the silicon film, followed by baking on a hotplate at 115 °C for 60 seconds. The metasurface pattern was defined using a maskless photolithography, and the samples were then developed for 60 seconds. An additional step of baking was carried out to harden the photoresist at 120 °C for 120 seconds before the etching process using deep reactive ion etching. The fabrication completed after performing the deep reactive ion etching.

Measurements. The measurements of transmission spectra were performed using a commercial THz-TDS, equipped with a pair of fiber-based THz transmitter and receiver. The transmitted intensity spectra were calculated by the formula $T(\omega) = |T_S(\omega)/T_{air}(\omega)|^2$, where $T_S(\omega)$ and $T_{air}(\omega)$ are the Fourier transforms of the time-domain signals of the samples and air reference, respectively. The setup was reconfigured with four parabolic mirrors yielding a uniformly collimated THz beam with a diameter of 10 mm for sensing and imaging measurements.

Data processing. The intensity spectra measured in far-field imaging experiments were normalized by adding a certain value to the entire spectra so that the maximal transmission intensity is 1. The data processing is to guarantee the same spectral baseline for different types of imaging targets, and the subsequent calculation of $\Delta T_i(\omega)$ was performed to retrieve the spatial pattern of targets. No other data processing was carried out except FFT in the near-field distributed sensing experiments.

References

1. Baker C, Lo T, Tribe WR et al. Detection of concealed explosives at a distance using terahertz technology. *Proc IEEE* **95**, 1559–1565 (2007).
2. Koch M, Mittleman DM, Ornik J et al. Terahertz time-domain spectroscopy. *Nat Rev Methods Primers* **3**, 49 (2023).
3. Cooper KB, Dengler RJ, Llombart N et al. THz imaging radar for standoff personnel screening. *IEEE Trans Terahertz Sci Technol* **1**, 169–182 (2011).
4. You XH, Wang CX, Huang J et al. Towards 6G wireless communication

networks: vision, enabling technologies, and new paradigm shifts. *Sci China Inf Sci* **64**, 110301 (2021).
5. Stantchev RI, Yu X, Blu T et al. Real-time terahertz imaging with a single-pixel detector. *Nat Commun* **11**, 2535 (2020).
6. Li XR, Li JX, Li YH et al. High-throughput terahertz imaging: progress and challenges. *Light Sci Appl* **12**, 233 (2023).
7. Poglitsch A, Waelkens C, Geis N et al. The photodetector array camera and spectrometer (PACS) on the herschel space observatory. *Astron Astrophys* **518**, L2 (2010).
8. Knap W, Teppe F, Meziani Y et al. Plasma wave detection of subterahertz and terahertz radiation by silicon field-effect transistors. *Appl Phys Lett* **85**, 675–677 (2004).
9. Watts CM, Shrekenhamer D, Montoya J et al. Terahertz compressive imaging with metamaterial spatial light modulators. *Nat Photonics* **8**, 605–609 (2014).
10. Olivieri L, Totero Gongora JS, Pasquazi A et al. Time-resolved nonlinear ghost imaging. *ACS Photonics* **5**, 3379–3388 (2018).
11. Edgar MP, Gibson GM, Padgett MJ. Principles and prospects for single-pixel imaging. *Nat Photonics* **13**, 13–20 (2019).
12. Chan WL, Charan K, Takhar D et al. A single-pixel terahertz imaging system based on compressed sensing. *Appl Phys Lett* **93**, 121105 (2008).
13. Chen SC, Feng Z, Li J et al. Ghost spintronic THz-emitter-array microscope. *Light Sci Appl* **9**, 99 (2020).
14. Olivieri L, Gongora JST, Peters L et al. Hyperspectral terahertz microscopy via nonlinear ghost imaging. *Optica* **7**, 186–191 (2020).
15. Zhao JP, E YW, Williams K et al. Spatial sampling of terahertz fields with sub-wavelength accuracy via probe-beam encoding. *Light Sci Appl* **8**, 55 (2019).
16. Shen H, Gan L, Newman N et al. Spinning disk for compressive imaging. *Opt Lett* **37**, 46–48 (2012).
17. Guan HH, Li DW, Park HC et al. Deep-learning two-photon fiberscopy for video-rate brain imaging in freely-behaving mice. *Nat Commun* **13**, 1534 (2022).
18. Zhang WY, Song HY, He X et al. Deeply learned broadband encoding stochastic hyperspectral imaging. *Light Sci Appl* **10**, 108 (2021).
19. Huang LQ, Luo RC, Liu X et al. Spectral imaging with deep learning. *Light Sci Appl* **11**, 61 (2022).
20. Williams C, Rughoobur G, Flewitt AJ et al. Nanostructured plasmonic metapixels. *Sci Rep* **7**, 7745 (2017).
21. Yesilkoy F, Arvelo ER, Jahani Y et al. Ultrasensitive hyperspectral imaging and biodetection enabled by dielectric metasurfaces. *Nat Photonics* **13**, 390–396 (2019).
22. Leitis A, Tittl A, Liu MK et al. Angle-multiplexed all-dielectric metasurfaces for broadband molecular fingerprint retrieval. *Sci Adv* **5**, eaaw2871 (2019).
23. Hsu CW, Zhen B, Stone AD et al. Bound states in the continuum. *Nat Rev Mater* **1**, 16048 (2016).
24. Xu GZ, Xing HY, Xue ZQ et al. Recent advances and perspective of photonic bound states in the continuum. *Ultrafast Sci* **3**, 0033 (2023).
25. Fan JX, Li ZL, Xue ZQ et al. Hybrid bound states in the continuum in terahertz metasurfaces. *Opto-Electron Sci* **2**, 230006 (2023).
26. Joseph S, Pandey S, Sarkar S et al. Bound states in the continuum in resonant nanostructures: an overview of engineered materials for tailored applications. *Nanophotonics* **10**, 4175–4207 (2021).
27. Tittl A, Leitis A, Liu MK et al. Imaging-based molecular barcoding with pixelated dielectric metasurfaces. *Science* **360**, 1105–1109 (2018).
28. Kodigala A, Lepetit T, Gu Q et al. Lasing action from photonic bound states in continuum. *Nature* **541**, 196–199 (2017).
29. Hwang MS, Lee HC, Kim KH et al. Ultralow-threshold laser using super-bound states in the continuum. *Nat Commun* **12**, 4135 (2021).
30. Saadatmand SB, Ahmadi V, Hamidi SM. Quasi-BIC based all-dielectric metasurfaces for ultra-sensitive refractive index and temperature sensing. *Sci Rep* **13**, 20625 (2023).
31. Azzam SI, Kildishev AV. Photonic bound states in the continuum: from basics to applications. *Adv Opt Mater* **9**, 2001469 (2021).
32. Koshelev K, Lepeshov S, Liu MK et al. Asymmetric metasurfaces with high-*Q* resonances governed by bound states in the continuum. *Phys Rev Lett* **121**, 193903 (2018).
33. Rybin M, Kivshar Y. Supercavity lasing. *Nature* **541**, 164–165 (2017).
34. Liu ZJ, Wang JY, Chen B et al. Giant enhancement of continuous wave second harmonic generation from few-layer GaSe coupled to high-*Q* quasi bound states in the continuum. *Nano Lett* **21**, 7405–7410 (2021).
35. Hu ZC, Bongiovanni D, Jukić D et al. Nonlinear control of photonic higher-order topological bound states in the continuum. *Light Sci Appl* **10**, 164 (2021).
36. Wang YL, Han ZH, Du Y et al. Ultrasensitive terahertz sensing with high-*Q* toroidal dipole resonance governed by bound states in the continuum in all-dielectric metasurface. *Nanophotonics* **10**, 1295–1307 (2021).
37. Jahani Y, Arvelo ER, Yesilkoy F et al. Imaging-based spectrometer-less optofluidic biosensors based on dielectric metasurfaces for detecting extracellular vesicles. *Nat Commun* **12**, 3246 (2021).
38. Fan JX, Zhou Y, Xue ZQ et al. Active singularity metadevices enabled by bound states in the continuum. *Laser Photonics Rev* **19**, 2401869 (2025).
39. Luo M, Zhou Y, Zhao XY et al. High-sensitivity optical sensors empowered by quasi-bound states in the continuum in a hybrid metal-dielectric metasurface. *ACS Nano* **18**, 6477–6486 (2024).
40. Ni B, Chu GH, Xu ZY et al. High Q-factor, high contrast, and multi-band optical sensor based on plasmonic square bracket dimer metasurface. *Nanomaterials* **14**, 421 (2024).
41. Haija AJ, Larry Freeman W, Umbel R. Review of the characteristic effective medium approximation: fundamentals and use in calculating the optical properties of ultrathin layer structures. *Phys B Condensed Matter* **406**, 4266–4271 (2011).
42. Dutta B, Root K, Ullmann I et al. Deep learning for terahertz image denoising in nondestructive historical document analysis. *Sci Rep* **12**, 22554 (2022).
43. Li XR, Mengu D, Yardimci NT et al. Plasmonic photoconductive terahertz focal-plane array with pixel super-resolution. *Nat Photonics* **18**, 139–148 (2024).
44. Jiang YY, Li GM, Ge HY et al. Machine learning and application in terahertz technology: a review on achievements and future challenges. *IEEE Access* **10**, 53761–53776 (2022).

Acknowledgements

This work was supported by the National Natural Science Foundation of China (Award Nos. 62335011, 62175099, 62505124), National Key R&D Program of China (Award No. 2024YFA1410100), Guangdong Basic and Applied Basic Research Foundation (Award No. 2023A1515011085), Guangdong Provincial Quantum Science Strategic Initiative (Award No. GDZX2406003), Shenzhen Science and Technology Program (Award No. JCYJ20241202125300002, JCYJ20230807093617036), and High level of special funds from Southern University of Science and Technology (Nos. G030230001, G03034K004). The authors acknowledge the assistance from Rui Zhang and Yao Wang of SUSTech Core Research Facilities.

Author contributions

L. C. and Y. Z. initiated the idea and supervised the project. Z. X., J. C. and Y. Z. fabricated samples. Z. X. performed experiments, simulations, analyzed data, and initiated the manuscript with G. X. and J. C. All authors read and commented on the manuscript.

Competing interests

The authors declare no competing financial interests.

Supplementary information

Supplementary information for this paper is available at https://doi.org/10.29026/oea.2026.250211